www.sciencemag.org/cgi/content/full/science.aaf9717/DC1

# Supplementary Materials for

## Perovskite-perovskite tandem photovoltaics with optimized bandgaps

Giles E. Eperon, Tomas Leijtens, Kevin A. Bush, Rohit Prasanna, Thomas Green, Jacob Tse-Wei Wang, David P. McMeekin, George Volonakis, Rebecca L. Milot, Richard May, Axel Palmstrom, Daniel J. Slotcavage, Rebecca A. Belisle, Jay B. Patel, Elizabeth S. Parrott, Rebecca J. Sutton, Wen Ma, Farhad Moghadam, Bert Conings, Aslihan Babayigit, Hans-Gerd Boyen, Stacey Bent, Feliciano Giustino, Laura M. Herz, Michael B. Johnston, Michael D. McGehee,* Henry J. Snaith*

*Corresponding author. Email: mmcgehee@stanford.edu (M.D.M.);
henry.snaith@physics.ox.ac.uk (H.J.S.)

Published 20 October 2016 on *Science* First Release
DOI: 10.1126/science.aaf9717

**This PDF file includes:**

- Materials and Methods
- Supplementary Text
- Figs. S1 to S21
- Tables S1 and S2
- References

## Materials and Methods

Unless otherwise stated, all materials were purchased from Sigma-Aldrich or Alfa Aesar and used as received.

### Perovskite precursor synthesis

Formamidinium iodide (FAI) was synthesized by dissolving formamidinium acetate powder in a 1.5x molar excess of 57% w/w hydroiodic acid (HI). After addition of acid the solution was left stirring for 10 minutes at 50°C. Upon drying at 100°C for 2h, a yellow-white powder is formed. This was then washed three times with diethyl ether. The power was then dissolved in ethanol heated at 80°C to obtain a supersaturated solution. Once fully dissolved, the solution is then placed in a refrigerator for overnight recrystallization. The recrystallization process forms white needle-like crystals. The powder is then washed with diethyl ether three times. Finally, the powder is dried overnight in a vacuum oven at 50°C.

### $FASn_xPb_{1-x}I_3$ precursor solution

To make the perovskite films, initially precursor solutions of $FASnI_3$ and $FAPbI_3$ were prepared and mixed in the appropriate ratio. $FASnI_3$ and $FAPbI_3$ solutions were prepared at a concentration of 1M in a mixed solvent of DMF:DMSO 65:35 by volume. The solutions were dissolved at 1:1 by moles FAI to $SnI_2$/$PbI_2$. In addition, excess $SnF_2$ was added into the tin precursor at 0.2M (i.e. providing a 20% excess of tin). This has been previously reported by several groups to retard oxidation of the $Sn^{2+}$ to Sn4+.(*4*, *33*, *34*) The solutions were stirred until dissolved and filtered with a 0.45um PTFE filter before use. They are stable for many weeks in nitrogen.

### $FASn_xPb_{1-x}I_3$ film formation

The precursor solution made by mixing the Pb and Sn precursors prepared as described above was spin-coated dynamically at 7000rpm for 1s in a nitrogen-filled glovebox, forming a wet transparent film. This film is then immediately immersed into a small petri dish containing anisole for ~5 seconds. It will now have formed a reddish or transparent precursor film, containing some DMSO, probably in the form of a DMSO complex. This film is taken out of the anisole and blow-dried with a nitrogen gun before annealing at 70°C for 20 minutes. This forms uniform, shiny black-brown films of the perovskite. For the pure Pb films, annealing at 170°C for 10 minutes was necessary to form the black phase perovskite; it formed the yellow phase when heated only at 70°C.

### Other film fabrication routes

A wide array of deposition conditions were used to deposit $FASnI_3$ films to try to achieve smooth and uniform films. For those specific films shown in the SI, Fig S1, the conditions used were:

Single-step spincoat: FAI and $SnI_2$ dissolved in DMF at 1M, spincoated at 2000rpm. Annealed at 70°C for 10 min.

2-step spincoat: SnI2 0.5M in DMF was spincoated at 2000rpm, then 20mg/ml FAI in IPA applied dynamically at 2000rpm. Annealed at 70°C for 10 min.

2-step dip conversion: $SnI_2$ 0.5M in DMF was spincoated at 2000rpm, then dipped into 10mg/ml FAI in IPA for 10 minutes. Annealed at 70°C for 10 min.

## Computational Methods

All density functional theory calculations were performed using the QUANTUM ESPRESSO package.(*35*) The PBE (Perdew, Burke, Ernzerhof) generalized gradient approximation was used to describe exchange–correlation effects.(*36*) Norm conserving, fully relativistic pseudopotentials were employed for Pb, Sn and I.(*37*) The kinetic energy cutoff was set at 80 and 320 Ry for the wavefunctions and the charge density, respectively. The convergence threshold used for both forces and total energy was $10^{-4}$ au. The Brillouin zone was sampled using a 6x6x6 uniform *k*-point grid for all the DFT-PBE (DFT = Density Functional Theory) calculations.

We also performed a set of calculations using the PBE0 hybrid functional (see reference).(*38*) For the DFT-PBE0 a 4x4x4 *k*-point grid was employed and a single *q*-point for sampling the Fock operator. Spin-orbit coupling was taken into account for the PBE0 calculations. In order to obtain PBE0 corrections for the mixed compounds, we have performed PBE0 calculations for $APbI_3$ and $ASnI_3$ and calculated bandgaps of 1.62 and 1.24 eV, respectively. We then linearly extrapolated the PBE0 correction for each of the mixed compounds. This correction was then added to the calculated PBE bandgaps both for the VCA and and the supercell calculations.

To model $FASn_xPb_{x-1}I_3$ we used the experimentally observed compositions. The lattice parameters for all calculations were fixed at the experimental values (see Table S1) and the atomic coordinates were fully optimized.

## Perovskite single-junction solar cell fabrication

Perovskite solar cells were fabricated in the inverted planar architecture: ITO/PEDOT:PSS/perovskite/$C_{60}$/BCP/Ag or Au. Devices were fabricated on pre-patterned Indium Tin Oxide (ITO) coated glass ($10\Omega\ \square^{-1}$). Substrates were then cleaned sequentially with Extran detergent, DI water, and propan-2-ol. A thin layer of PEDOT:PSS (Clevios, P VP Al4083) was deposited by diluting in a 1:1 ratio by volume with methanol, filtering with a 0.45um glass fibre filter, and spin-coating in air at 4500rpm for 40s. This was then annealed at 120°C for 15 minutes.

Subsequently, the substrates were taken into a nitrogen-filled glovebox and not exposed to air until testing. For the optimized devices discussed in Figures 2-3, the perovskite was then deposited by spin coating 1.1M stoichiometric solutions made as described above of $FASn_xPb_{x-1}I_3$ and $FA_{0.75}Cs_{0.25}Pb_{0.5}Sn_{0.5}I_3$. 30 ul of solution was dropped onto the substrates, which were then spun at 11000 r.p.m. (12000 r.p.m./s acceleration) for 1 second. The substrate then underwent a 22 second deceleration (500 r.p.m./s) to 0 r.p.m. It was then rapidly placed in a bath of anisole for ~5 seconds, after which it was dried with $N_2$ gas. Each sample was left at room temperature for 5 minutes before annealing at 70 °C for 20 minutes.

For the thicker (330 nm) $FA_{0.75}Cs_{0.25}Pb_{0.5}Sn_{0.5}I_3$ devices, the spin coating parameters were changed. Here, we dropped 30 ul of solution onto the substrate and spun at 3000 r.p.m. (3000 r.p.m./s acceleration) for 20 seconds. After 17 seconds, we dropped 200 µl of anisole onto the substrate. Once the substrate had stopped spinning, they were immersed in anisole for 5 seconds, dried with an $N_2$ gas flow, and left for 5 minutes at RT before annealing at 70 C for 20 minutes.

$C_{60}$ (40 nm), bathcuproine (7 nm), were then thermally evaporated onto the perovskite for the devices reported in Figures 2-3.

For the non optimized devices in Figure S8, a solution of PCBM (Solenne BV) dissolved in chlorobenzene at 30mg/ml was spin-coated dynamically on the perovskite at 2000rpm for 30s. Subsequently a solution of bathcuproine of 0.5mg/ml in anhydrous propan-2-ol was spin-coated dynamically at 6000rpm for 15s.

To complete the devices, silver or gold (for stability tests) was thermally evaporated onto the film at an initial rate of 0.3 angstrom/s, ramping up to 1 angstrom/s, to form a layer of 80-120nm thickness. Performance of the best devices with Ag and Au were similar.

We note that similar devices were made in two labs (Oxford and Stanford), and following the same procedures performance was very similar, indicating good lab-to-lab reproducibility of these materials.

### Device characterization: solar simulator measurements

### $FAPb_{0.5}Sn_{0.5}I_3$ and $FA_{0.75}Cs_{0.25}Pb_{0.5}Sn_{0.5}I_3$ devices

The current density–voltage (J-V) curves were measured (2400 Series SourceMeter, Keithley Instruments) in air under simulated AM 1.5 sunlight at 100 mWcm-2 irradiance generated by an Abet Class AAB sun 2000 simulator, with the intensity calibrated with an NREL calibrated KG5 filtered Si reference cell. The masked area of the solar cell is 0.12 $cm^{-2}$ unless stated otherwise. The forward J–V scans were measured from forward bias (FB) to short circuit (SC) and the backward scans were from short circuit to forward bias, both at a scan rate of $0.38Vs_{-1}$. There was no stabilization, pre-biasing or light soaking prior to measurement.

We note that most xenon solar simulators have intensity spikes in the near infra-red region, so care must be taken to determine a mismatch factor for materials with bandgaps lower than about 1.3eV and correct the illumination accordingly. In this case, the mismatch (10%) necessitated modifying the light intensity to ensure that the devices were actually receiving AM1.5 100mWcm-2 illumination(*39*). For all of the device measurements for the small bandgap cells in this paper, we calibrated our solar simulator according to mismatch and checked it with a silicon photodiode filtered by a 1.2 eV cutoff filter.

The maximum power point of the devices was monitored over time using a maximum power point tracking software to obtain the stabilized power output (SPO) of the solar cells.

### $FASn_xPb_{1-x}I_3$ devices

The devices with varying tin percentage (Fig. S8) were measured in the same way except under nitrogen, as their air stability was unknown. Illumination was done with a white LED outputting $93mWcm^{-2}$; current was subsequently adjusted to the calibrated value determined by EQE measurement.

### $FA_{0.83}Cs_{0.13}Pb(I_{0.5}Br_{0.5})_3$ devices

The 1.8 eV perovskite devices were made on ITO substrates which were cleaned as described above. $NiO_x$ layers were deposited by spin coating (5500 r.p.m. for 60 seconds in air) a 1M solution of Nickel Nitrate and Diethylamine in Ethylene Glycol directly from a 0.4 um PTFE filter tip. The substrates were then dried at 100 °C for 10 minutes prior to annealing at 300 °C for 1 hour. A 1.5M stoichiometric solution in 65:35 DMF:DMSO by volume was spin coated at 6500 r.p.m. (12000 r.p.m./s) for 2 seconds, followed by a 15 second deceleration (500 rpm/s) to 0 rpm. The films are then immersed in anisole for 5 seconds, dried with $N_2$ gas, and dried at 50 °C for 3 minutes, followed by 150 °C for 5 minutes. PCBM (10 nm) was evaporated on top of the perovskite. A thin 4 nm tin oxide/2 nm zinc-tin-oxide layer stack was deposited on top to protect from sputter damage. This was accomplished by  using a combination of tin oxide and zinc oxide atomic layer deposition processes at 100 °C with tetrakis(dimethylamino) tin(IV) and diethyl zinc as the respective metal organic precursors and water as the oxidizer, as described in our previous work.(*29*)

For opaque devices presented in Figure S13, 100 nm of Al was thermally evaporated on top.

### 1.6eV devices

A stoichiometric 1.1M (in 80:20 DMF:DMSO) solution of $FA_{0.83}Cs_{0.17}Pb(I_{0.83}Br_{0.17})_3$ with 10% M excess $PbI_2$ was spin coated at 1000 rpm for 10 seconds, followed by 6000 rpm for 30 seconds.(*2*) 5 seconds from the end, 100 ul of chlorobenzene was dropped onto the spinning sample. The device was then annealed at 100 °C for 30 minutes. PCBM, tin oxide, and ITO were deposited as above and below.

### 2T Tandem devices

The 1.8eV front cells were prepared as described above, but instead of Al, 100 nm of indium tin oxide was sputtered on top of the finished cell. The ITO was sputtered with a base pressure of 5 $x10^{-6}$ torr, with $2x10^{-3}$ torr deposition pressure and 5% oxygen partial pressure and a power density of 8 W $in^2$. The devices were post-annealed at 120 C for 10 minutes. They were then cleaned in UV-ozone for 15 minutes, after which PEDOT:PSS was spin coated on top as described above. The rear cell was then prepared exactly as described above for the $FA_{0.75}Cs_{0.25}Pb_{0.5}Sn_{0.5}I_3$ devices. The device layout is given in Figure S14 and includes a thermally evaporated $MgF_2$ strip to prevent the two ITO layers from .contacting each other after any possible dissolution of the 1.8eV solar cell during the solution processing of the 1.2eV solar cell on top.

### EQE measurements

External quantum efficiency (EQE) was measured in a home built setup. Light from a Xenon lamp was monochromated, optically chopped at 73 Hz, and directed onto the sample. The light intensity was calibrated with a silicon photodiode of known EQE. The light beam was split between sample and a Si diode reference to take into account any fluctuations in light intensity. The photocurrent current of the sample, calibration diode, and reference diode were all measured with a lock-in amplifier set to the same frequency as the optical chopper. The beam spot was smaller than the device pixel.

The EQEs of the 2T tandem devices were measured by contacting the front and rear cells individually, which is enabled by the fact that the recombination layer is an ITO layer, conductive enough to function as an electrode in its own right. This technique has been previously detailed.(*40*) We show a schematic of the contacting scheme in Fig S20.

### EQE measurements for $FASn_xPb_{1-x}I_3$ devices in Fig. S8

External quantum efficiency was measured in a nitrogen chamber via fourier transform photocurrent spectroscopy. This was carried out using the modulated beam of a Bruker Vertex 80v Fourier Transform Interferometer with tungsten lamp source and a Stanford Research SR570 current preamplifier. Samples were calibrated to a Newport-calibrated reference silicon solar cell with a known external quantum efficiency. The solar cells were masked with a metal aperture to define the active area, typically $0.0919cm^{-2}$.

### Photoluminescence measurements

Samples were excited using a tunable Ti:Sapphire pulsed (80 fs) laser with a wavelength of 800 nm and an 80 MHz repetition rate (Mai Tai, Spectra-Physics). A BBO crystal was used to double the excitation frequency, giving a wavelength of 400 nm. The 800 nm fundamental wavelength was filtered out using a polariser and a colour filter. The excitation intensity was attenuated down to 500 µW over an area of 0.2 $mm^2$ to give a fluence of approximately 3 $nJcm^{-2}$ and vertically polarised. A horizontal polariser and a 550-nm long-pass colour filter were placed after the sample to remove any laser scatter from the spectrum. Photoluminescence from the sample was collected by a pair of off-axis parabolic mirrors and focused onto the entry slit of a grating monochromator (Triax, Horiba). The spectrally resolved PL was detected by a nitrogen-cooled Si-CCD detector (Symphony, Horiba) and the spectral response of the detector was corrected for using a tungsten filament lamp with known spectrum. This is particularly important for tin perovskites since the sensitivity of the CCD drops off in the NIR where these materials emit.

### Fourier transform infrared spectroscopy

Samples were prepared on KBr substrates. FTIR was carried out using the modulated beam of a Bruker Vertex 80v Fourier Transform Interferometer with tungsten lamp source as describe previosuly.(*41*) Infrared spectra were measured using a Bruker Vertex 80v Fourier-transform infrared (FTIR) spectrometer fitted with a transmission accessory. Mid-infrared measurements were taken using a globar source and a nitrogen-cooled photovoltaic HgCdTe detector. Samples were prepared with different annealing times and measured rapidly to prevent any evaporation of DMSO. Samples were held under nitrogen at all times between film formation and during measurement.

### Film characterization

A Hitachi S-4300 field emission scanning electron microscope was used to acquire SEM images.

A PANalytical Empyrean $PIXcel^{1D}$ diffractometer with Cu anode was used to obtain XRD measurements under $N_2$.

A Perkin-Elmer Lambda 1050 UV/Vis/NIR spectrophotometer in transmission mode was used to obtain absorbance spectra.

### Tauc plot bandgap determination

Bandgap was estimated by plotting $(\alpha h\nu)^2$ against hν, where α is the absorption coefficient of the material, extracted from absorbance measurements. We assumed these materials had a direct bandgap, as has been shown for halide perovskite semiconductors studied previously, hence the use of 2 as the exponent.

We note that we did not use an integrating sphere when measuring absorbance. This means that the absorbance spectrum will include a contribution from scattering. Although scattering observed was small, its inclusion means that Tauc-determined absorption onsets must be taken only as an estimation – they are likely to be slight underestimates.

### Optical-pump – THz probe spectroscopy

An amplified laser (Millennia-Tsunami-Empower-Spitfire from Spectra Physics) with a pulse duration of 40 fs, center wavelength of 800 nm, and repetition rate of 1.1 kHz was used to generate THz radiation via optical rectification in a 450 µm thick GaP(110) single crystal and detect it using free space electro-optic sampling in a ZnTe crystal (0.2 mm ZnTe(110) on 3 mm ZnTe(100)). Perovskite thin films deposited on z-cut quartz substrates were photoexcited at 800 nm with fluences ranging from 10 – 250 $\mu J/cm^2$ The change in THz amplitude was monitored as a function of the time delay between the 800-nm optical pump pulse and THz probe pulse in order to determine mobility, recombination dynamics, and diffusion length as described previously.(*42*)

### UPS and XPS

Valence band spectroscopy was carried out on a commercial electron spectrometer (PHI-5600LS) with an X-ray source providing monochromated Al-Kα photons (1486.6eV). Work functions were determined from the secondary electron cutoff of appropriate spectra measured with He-I radiation (21.2eV).

## Supplementary Text

### Computational Methods

In order to elucidate the mechanisms underpinning this anomalous bandgap trend, we performed first-principles calculations of band gaps as a function of the tin-lead ratio. Methods are described above. As a starting point we considered the measured trigonal and orthorhombic unit cells of $FAPbI_3$ and $FASnI_3$, respectively, and we replaced the FA molecules by Cs atoms in order to focus on the role of the inorganic framework. We have previously found that the A site cation plays no electronic role in determining the bandgap, rather it plays a structural role, which in turn affects the bandgap.(*43*) Given that we set the crystal structure of the materials considered according to fitted XRD experimental data, the A site cation used does not matter for this calculation.

To describe the Sn-Pb mixing we followed two alternative routes. In the first approach we employed the virtual crystal approximation (VCA), where the B-site cations in the $ABX_3$ perovskite structure were described as "virtual" atoms with mixed Pb and Sn character. This approach allows describes a random solid solution, and allows us to investigate the electronic structure of $ASn_xPb_{x-1}I_3$ by means of an average crystal structure which does not include the effects of local distortions and short- or intermediate-range ordering of the Sn/Pb cations.

In the second approach, we constructed a supercell containing eight $BX_6$ octahedra, and proceeded to the explicit replacement of B-site cations so as to achieve the desired Sn-Pb ratios. The inequivalent structures thus obtained are shown in Figure S6. This second approach allows us to probe the role of local distortions introduced by a short-range ordering of the cations.

Within the VCA, we found that the calculated band gaps decrease monotonically from Pb to Sn, as shown in Figure SX. The abrupt change of the band gap observed for concentrations x=62.5 to x=75 relates to the large volume decrease for these compounds (see Table S1). On the other hand, when including Pb and Sn cations within the supercell approach, an anomalous band gap trend emerges, very similar to our experimental data (see Figure S6 and Figure 1). This trend is observed only for compositions with more than 50% Sn, and for specific types of short-range ordering. From the comparison between our VCA and supercell calculations and experiment, we infer that the measured anomaly originates from local structural distortions as opposed to a continuous change of the electronic structure and the unit cell volume from Pb to Sn. Recently, Im et al. attributed a similar anomaly observed in the case of $MA(Pb,Sn)I_3$ to the competition between spin-orbit coupling and distortions of the lattice.(*11*) If this was indeed the origin of the gap anomaly, then it should be clearly observable in our VCA calculations (since the VCA captures both effects). However, as it is clear from Figure SX, the VCA does not exhibit any anomaly, therefore spin-orbit coupling is to be ruled out. Instead we propose that the (Pb,Sn) based mixed perovskites exhibit some degree of short-range order, that is on the length-scale of two/three octahedra.

The measured band gaps match well with the smallest band gaps calculated using the supercell approach. The structural motifs which yield band gap closest to experiment are those where Pb or Sn form atomic-scale clusters, such as for example nearest-neighbor pairs of PbI6 ochtahedra. From an energetic point of view, the various structural motifs shown in Figure S8 are energetically degenerate. In fact, the largest difference in total energy that we calculated is 2 meV per supercell, which is well below thermal energies. This suggests that our compounds contain various combinations of the motifs shown in Figure S8, but the absorption and emission onsets probed by UV-VIS and PL reflect the motif with the smallest gap. This observation is consistent with the shallow rise in the measured absorption onset reported in Fig. S4. We stress that the proposed short-range order is in the sub-nanoscale regime, and thus fully compatible with sample homogeneity at the nano- and micro-scales.

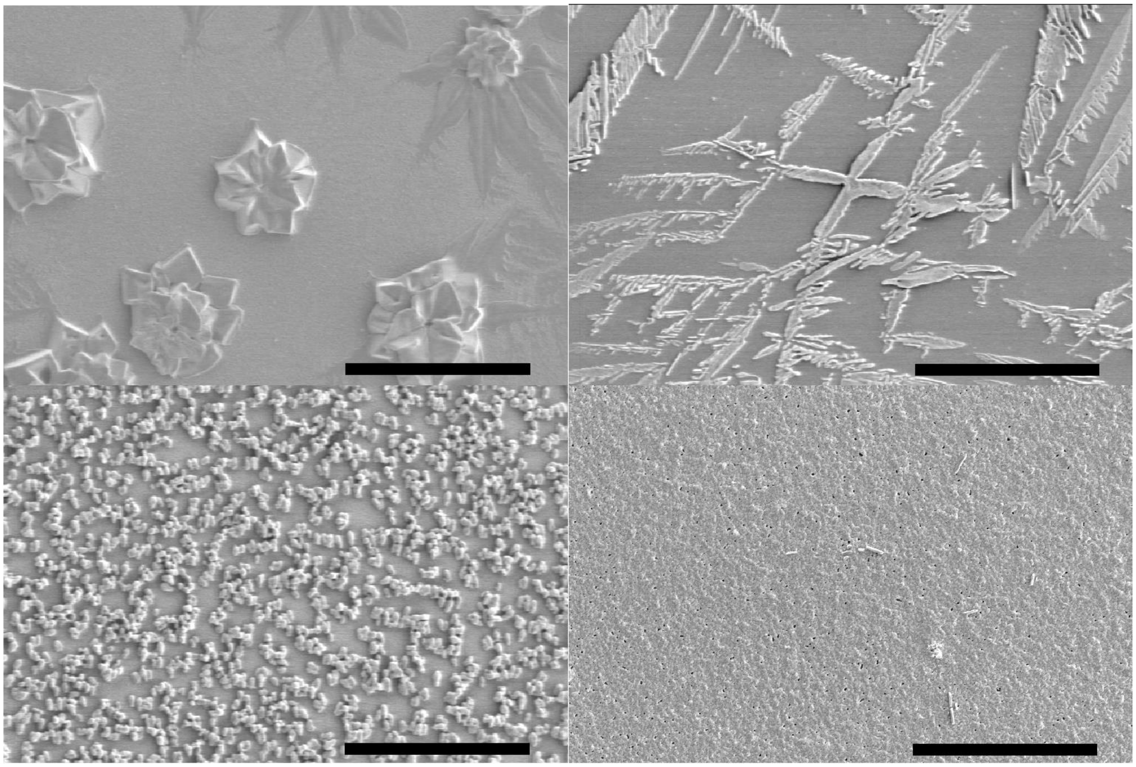

**Fig. S1.Scanning electron microscopy comparison of different deposition techniques for $FASnI_3$.** Top left: single-step spin-coating 1:1 FAI:$SnI_2$ in DMF. Top right: Two-step dipping $SnI_2$ film into FAI in propan-2-ol solution. Bottom left: 2-step spincoating FAI in propan-2-ol onto $SnI_2$ film. Bottom right: precursor phase antisolvent immersion. Scale bar is 20µm in all cases.

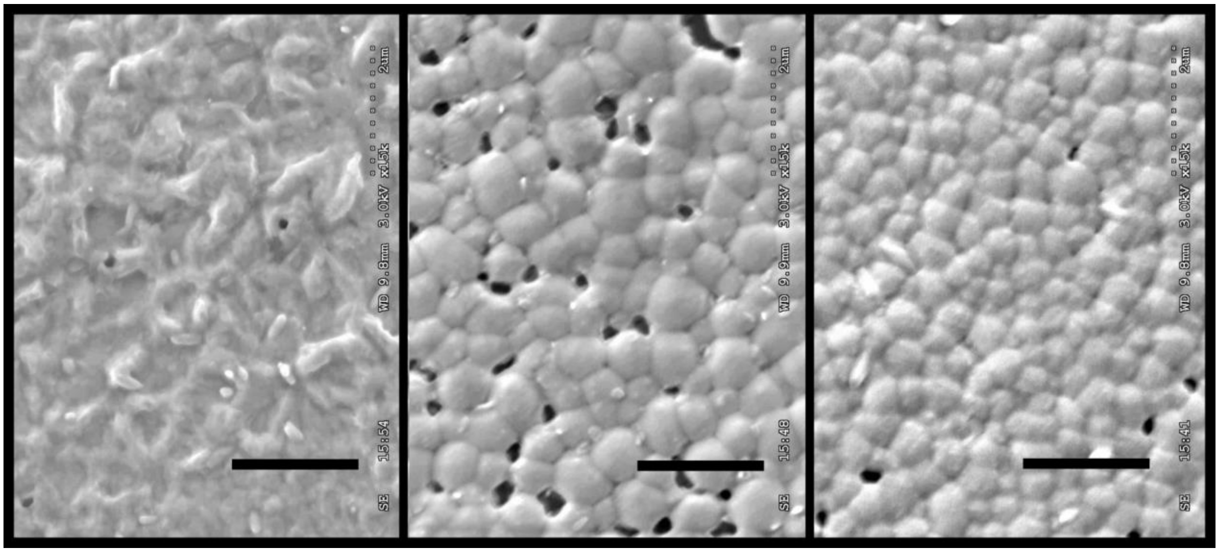

**Fig. S2. Scanning electron microscope images showing comparison of different solvents used as the quenching solvent, for FASnI$_3$.** Left to right: toluene, chlorobenzene, anisole. The scale bar is 2um in all cases.

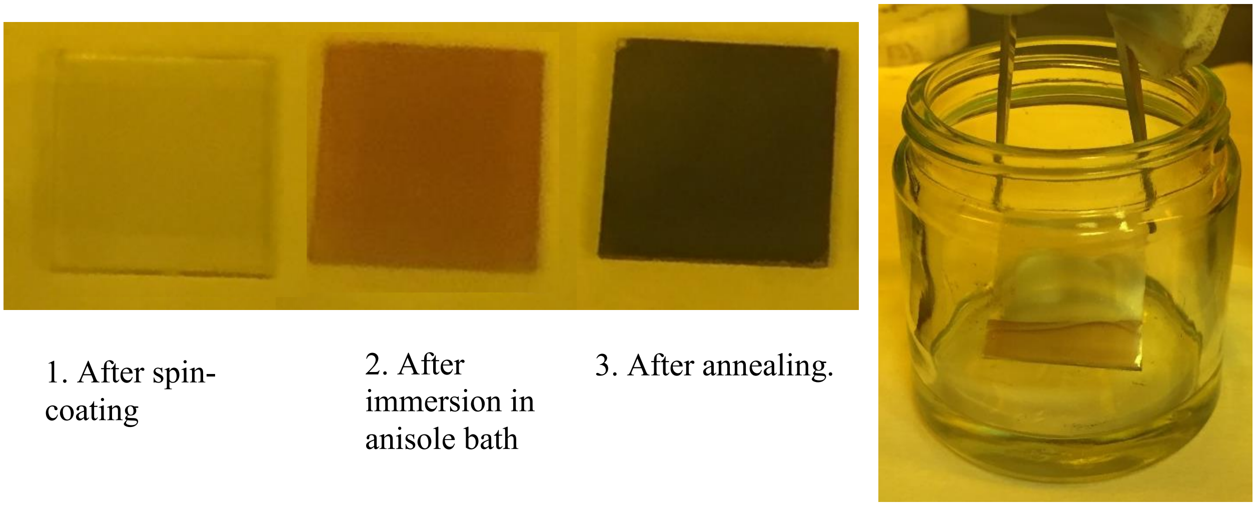

1. After spin-coating

2. After immersion in anisole bath

3. After annealing.

**Fig. S3. PAI.** Above: Photographs of $FASn_{0.5}Pb_{0.5}I_3$ films at different stages of the precursor phase antisolvent immersion deposition technique, showing change in colour of the films. Right: dipping into anisole bath in progress showing change from transparent to reddish colour.

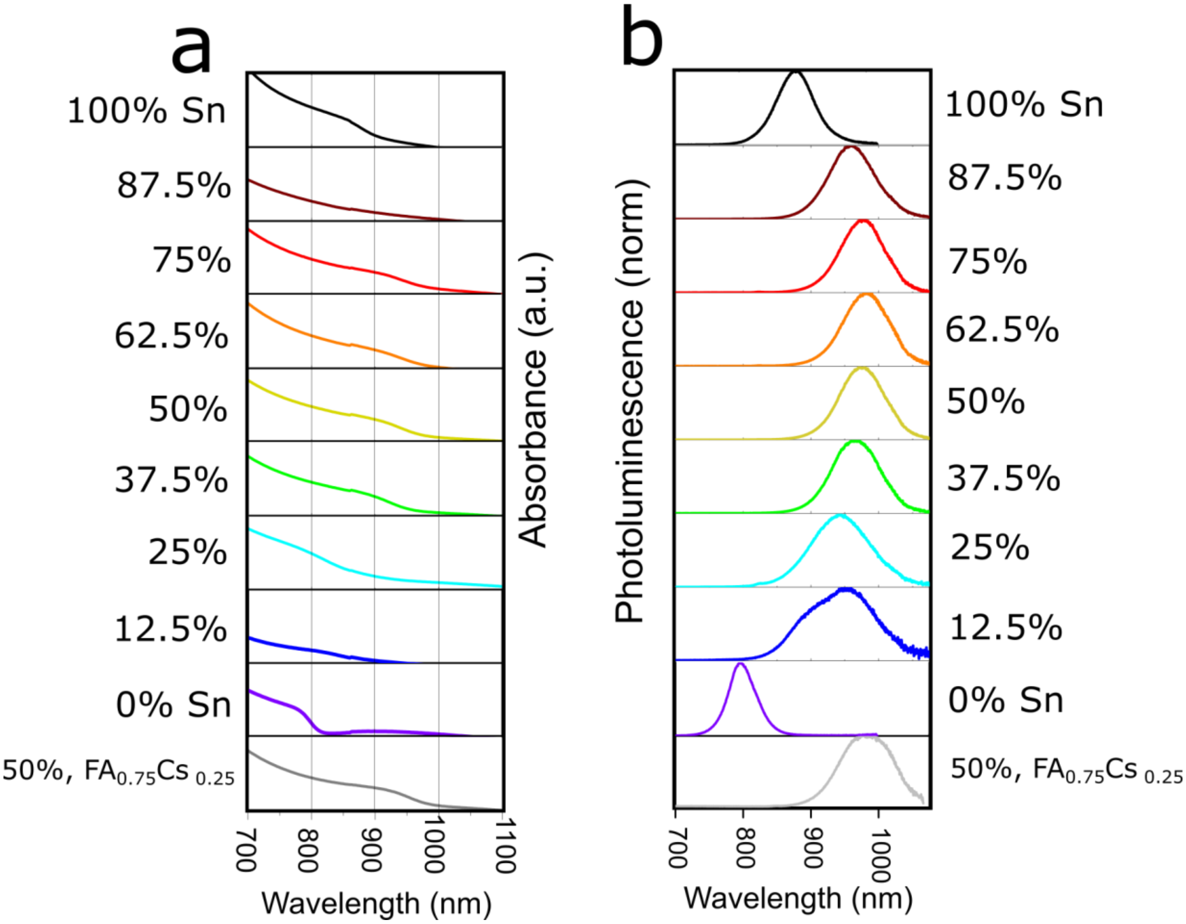

**Fig. S4: Optical characterization of $FASn_xPb_{1-x}I_3$ and $FA_{0.75}Cs_{0.25}Sn_{0.5}Pb_{0.5}I_3$. a***)* Absorption spectra of $FASn_xPb_{1-x}I_3$ films with varying Sn % and $FA_{0.75}Cs_{0.25}Pb_{0.5}Sn_{0.5}I_3$. b) Photoluminescence spectra of $FASn_xPb_{1-x}I_3$ films with varying Sn% and $FA_{0.75}Cs_{0.25}Pb_{0.5}Sn_{0.5}I_3$.

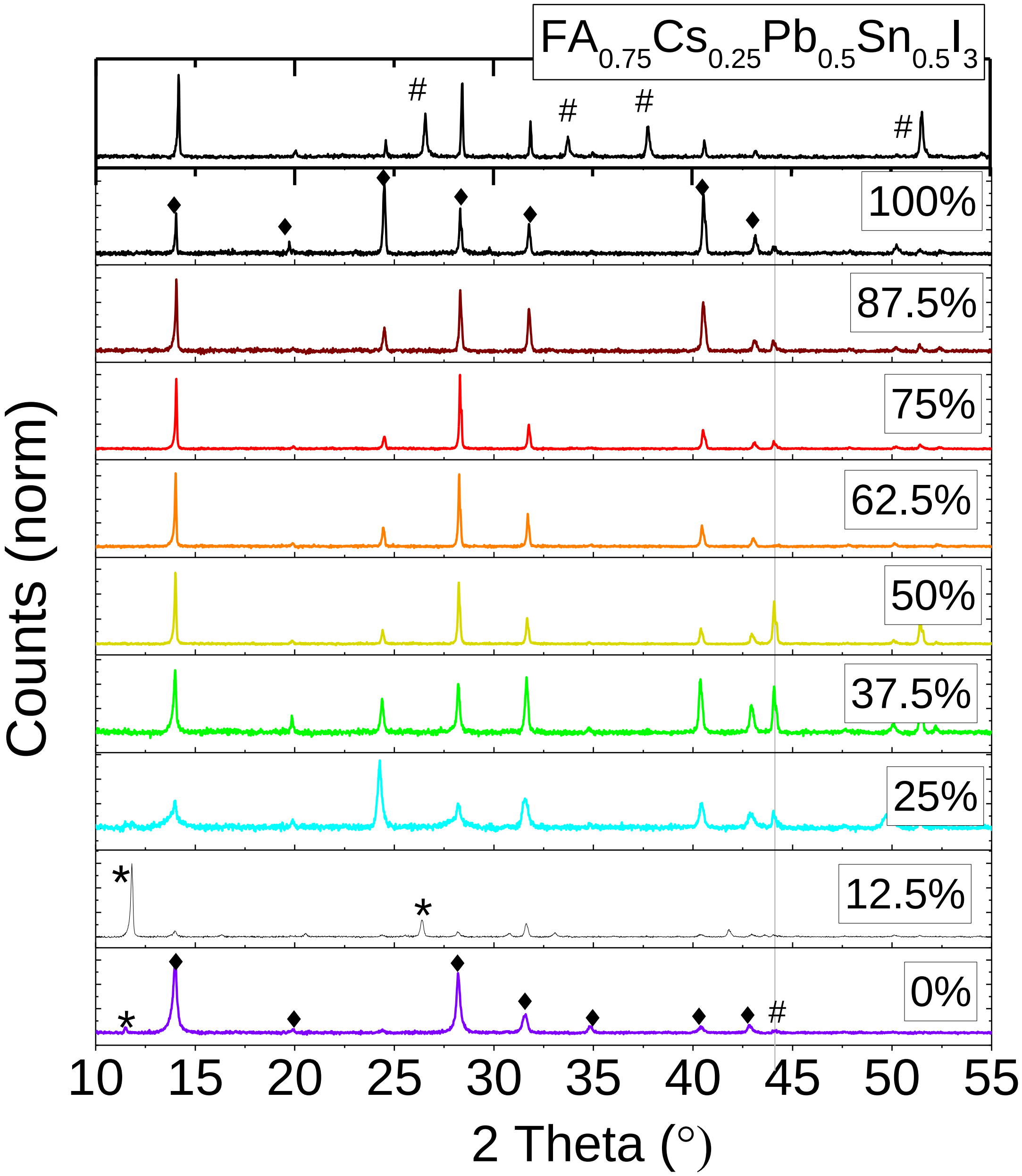

**Figure S5: X-ray diffraction spectra for thin films of the whole series of $FASn_xPb_{1-x}I_3$.** Peaks marked with a * are assigned to the known yellow phase for $FAPbI_3$. Peaks marked with a # are from the substrate (note that a different substrate was used for the Cs-containing material than the others). Peaks marked with a diamond are assigned to the known black phase perovskite peaks for FASnI3 and FAPbI3 respectively.(*10*, *34*)

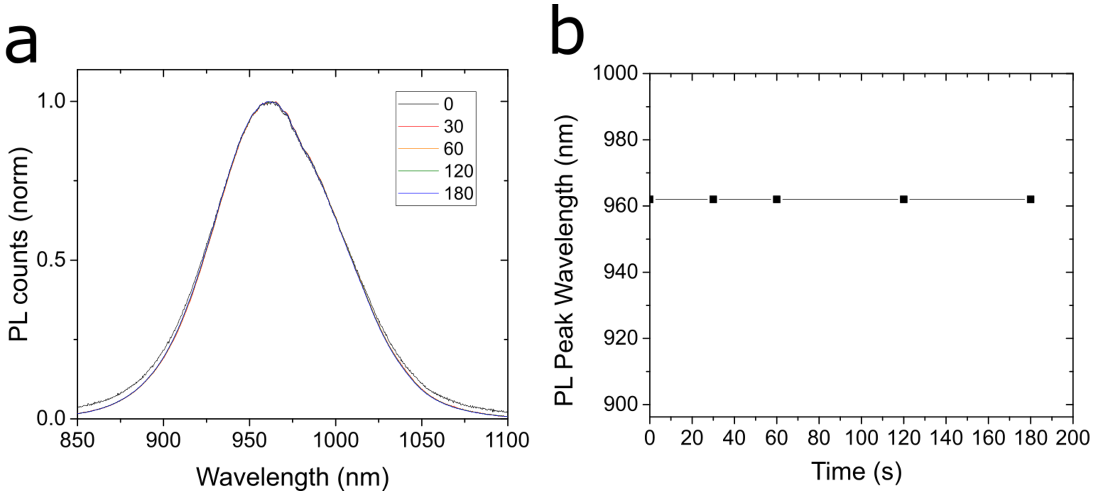

**Figure S6: PL stability of $FA_{0.75}Cs_{0.25}Sn_{0.5}Pb_{0.5}I_3$.** a) PL spectrum measured over time (seconds) on encapsulated sample in air, when illuminated with 375nm CW laser, 5mW, $1mm^2$ spot size (approx. 5-10 suns). b) Extracted PL peak position showing no change in PL peak wavelength over time.

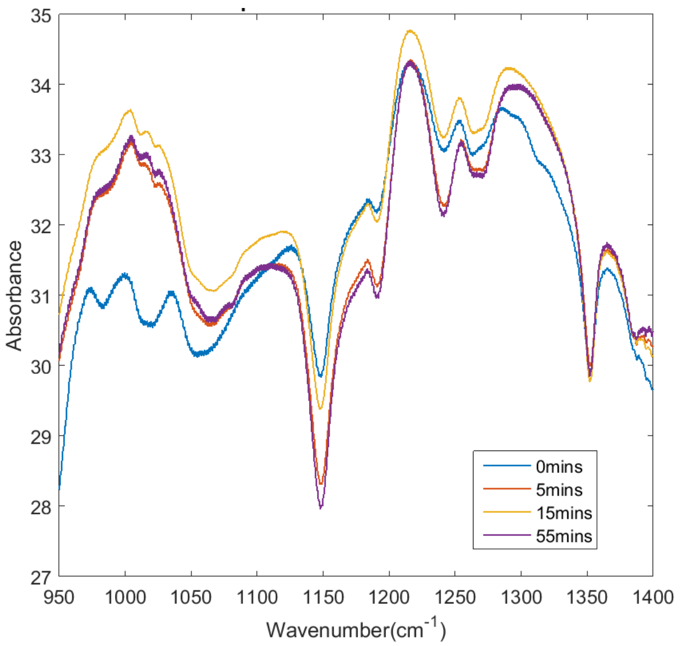

**Fig. S7: FTIR spectra of the FASnPbI3 perovskite film after dipping in anisole, for different anneal times, showing the complete removal of the DMSO peak after 5 mins annealing at 70°C.** DMSO has a representative absorption at ~1000cm$^{-1}$.

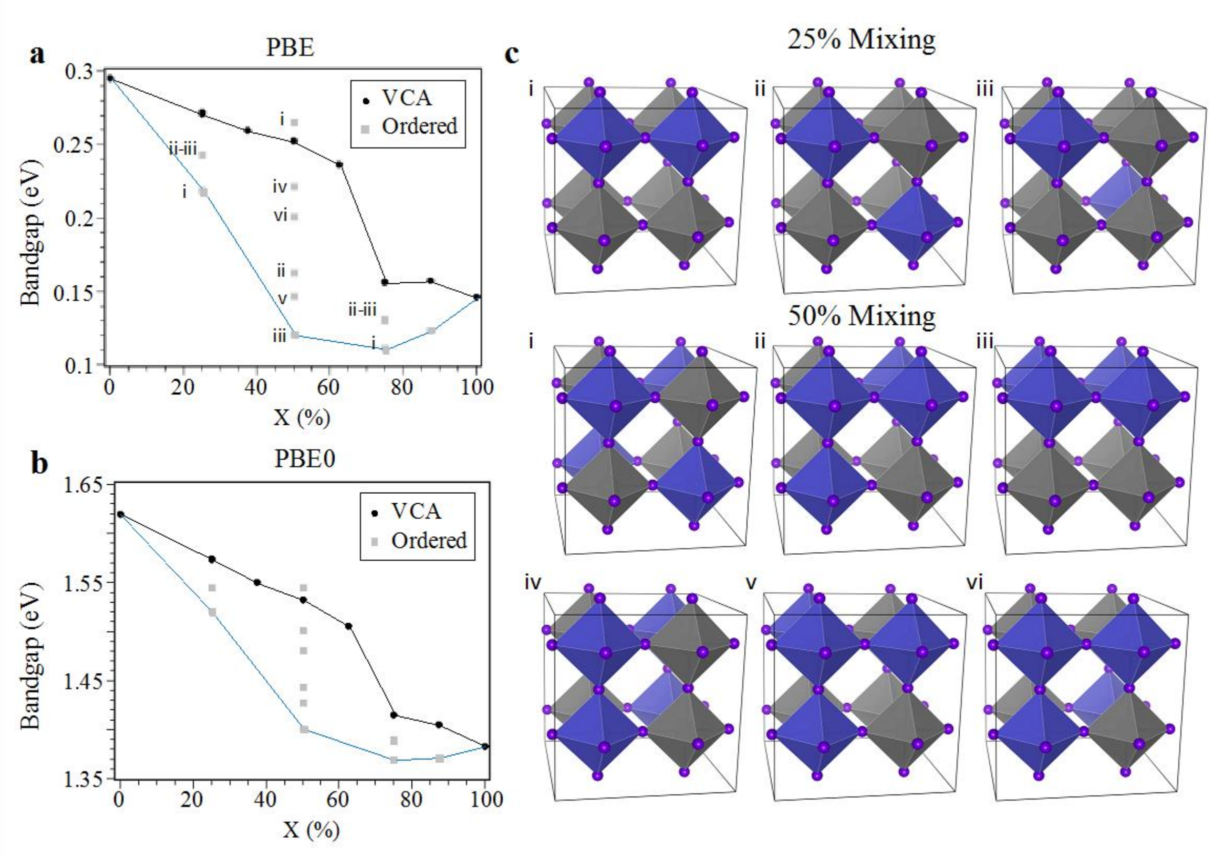

**Figure S8: Bandgaps calculated using the virtual crystal approximation (black circles) and using a supercell containing eight $BX_6$ octahedra (grey squares) within (a) the PBE and (b) the hybrid PBE0 functional.** The solid black line goes through the data points calculated within the VCA. The solid blue line goes through the smallest gaps calculated in the supercell approach. (c) Possible octahedra arrangement within an eight octahedra super-cell for the Sn/Pb ratios 25% and 50% Sn-Pb ratios. Blue octahedra are tin-containing, grey are lead. All possible arrangements have total energies within 2 meV per supercell. The A-site cations are not shown for clarity.

| **Sample** | **Space group** | **a** | **b** | **c** |
|---|---|---|---|---|
| 100Sn | Amm2 | 6.3134(8) | 8.936(10) | 8.9134(8) |
| 87.5Sn | Amm2 | 6.3225(2) | 8.9382(6) | 8.9219(7) |
| 75Sn | Amm2 | 6.3213(3) | 8.9349(8) | 8.912(1) |
| 62.5Sn | Amm2 | 6.4092(4) | 8.962(1) | 8.9402(5) |
| 50Sn | Amm2 | 6.4166(5) | 8.965(1) | 8.9508(9) |
| 37.5Sn | Amm2 | 6.4152(3) | 8.9608(8) | 8.948(1) |
| 25Sn | Amm2 | 6.4151(3) | 8.9606(9) | 8.942(1) |
| 25Sn | P3m1 | 8.979(6) | 8.979(6) | 11.035(6) |
| 0Sn | P3m1 | 8.966(5) | 8.966(5) | 11.01(1) |
| $FA_{0.75}Cs_{0.25}Sn_{0.5}Pb_{0.5}I_3$ | Amm2 | 6.4490(2) | 8.9254(1) | 8.9037(6) |

**Table S1. Structural refinements from X-ray diffraction data for $FASn_xPb_{1-x}I_3$ and $FA_{0.75}Cs_{0.25}Sn_{0.5}Pb_{0.5}I_3$.** The 25% Sn data fitted either P3m1 or Amm2 structures with a reasonable degree of fit so both are shown here for completeness. 12.5% Sn was dominated by the yellow phase so no fit was possible for the black phase material.

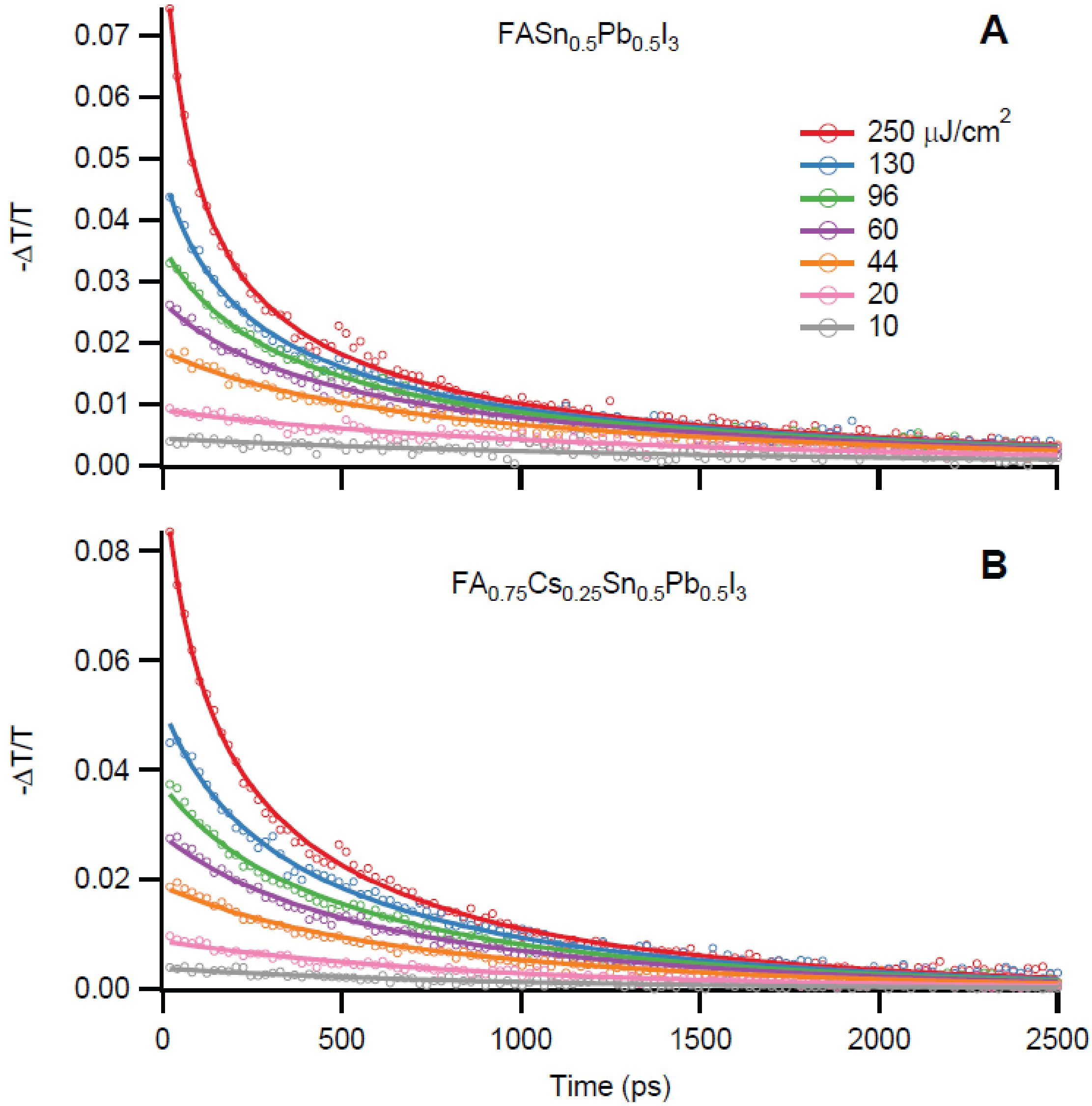

**Figure S9: Charge-carrier recombination dynamics in the 50% Sn sample following excitation at 800 nm with fluences ranging from 10 – 250 μJcm$^{-2}$.** Open circles are experimental data, and solid lines are fits to the rate equation $\frac{dn}{dt} = -k_3 n^3 - k_2 n^2 - k_1 n$, where $n$ is the charge-carrier density, $k_1$ is the monomolecular recombination rate, $k_2$ is the bimolecular rate constant, and $k_3$ is the Auger rate constant. A global fit was performed across all fluences, and the obtained values are summarized in the following table.

| | **$FASn_{0.5}Pb_{0.5}I_3$** | **$FA_{0.75}Cs_{0.25}Sn_{0.5}Pb_{0.5}I_3$** |
|---|---|---|
| **Mobility ($cm^2V^{-1}s^{-1}$)** | 17 | 14 |
| **$k_1$ ($s^{-1}$)** | $5 \times 10^8$ | $10 \times 10^8$ |
| **$k_2$ ($cm^3s^{-1}$)** | $1.4 \times 10^{-10}$ | $0.95 \times 10^{-10}$ |
| **$k_3$ ($cm^6s^{-1}$)** | $3.7 \times 10^{-29}$ | $1.8 \times 10^{-29}$ |
| **$L_D$ (µm)** | 0.21 | 0.19 |

**Table S2. Mobility, charge carrier recombination rate constants, and diffusion length obtained from optical pump – THz probe measurements.** The mobility values are determined using the maximum value of $\Delta T/T$ in the linear regime as described previously. The diffusion length ($L_D$) is calculated using $\boldsymbol{L_D(n) = \sqrt{D/R_{tot}(n)}}$, where the diffusion constant $\boldsymbol{D = \mu k_B T/e}$ and the total recombination rate $\boldsymbol{R_{tot} = -\frac{1}{n}\frac{dn}{dt} = n^2k_3 + nk_2 + k_1}$. A carrier density of $n = 10^{14}$ was used as representative of typical operating conditions for a solar cell. The reported values of the diffusion length are the average of 3-4 samples, and the mobility and recombination rate constants are obtained from one set of representative samples. The best samples showed diffusion lengths of 0.3 µm in both cases.

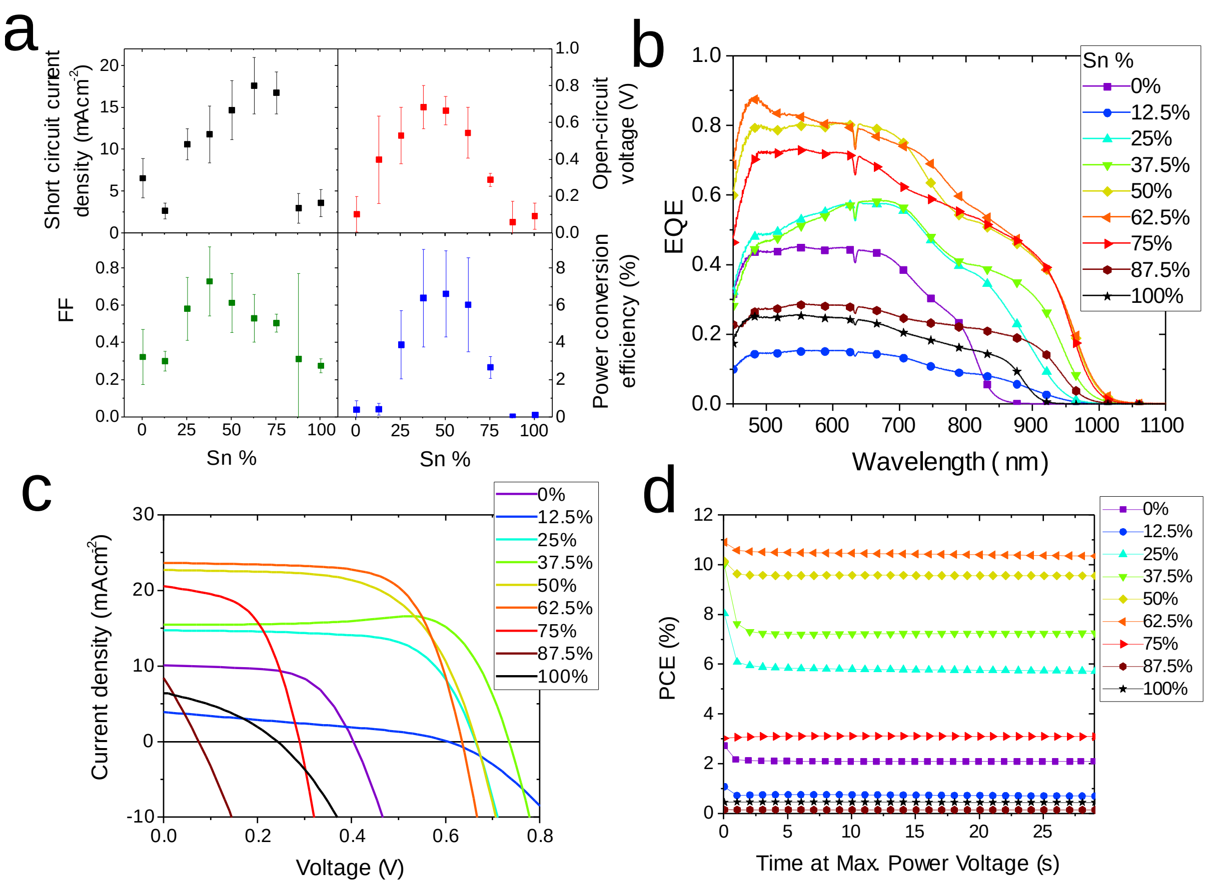

**Figure S10: a) Photovoltaic parameters as a function of Sn% composition for planar inverted perovskite solar cells measured in nitrogen with a 93mWcm-2 white LED.** 16 devices for each composition were tested, and error bars determined from the standard deviation. b) External quantum efficiency spectra for representative devices of each composition. c) Current-voltage characteristics for the best devices of each composition, measured under the same conditions as in a). d) stabilized power output over time when devices are held at the maximum power point voltage determined from the fast JV scans, showing little hysteresis and rapid stabilization. We note that although the champion 62.5% Sn device was best, on average the 50% Sn performed better.

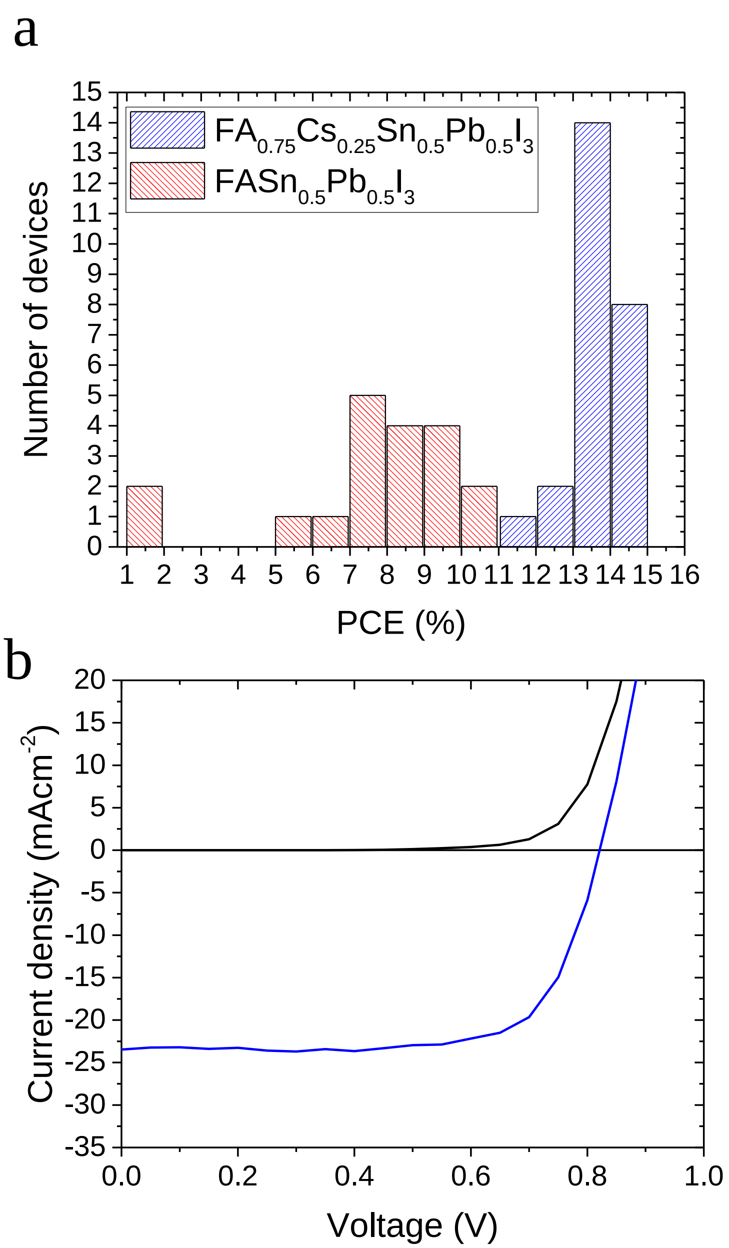

**Fig. S11: Cs addition.** a) Bar charts showing distribution of PCE values for a batch of 19 optimized $FASn_{0.5}Pb_{0.5}I_3$ devices and 24 optimized $FA_{0.75}Cs_{0.25}Sn_{0.5}Pb_{0.5}I_3$ devices. b) Current-voltage characteristics for highest voltage-attaining $FA_{0.75}Cs_{0.25}Sn_{0.5}Pb_{0.5}I_3$ device (0.83V).

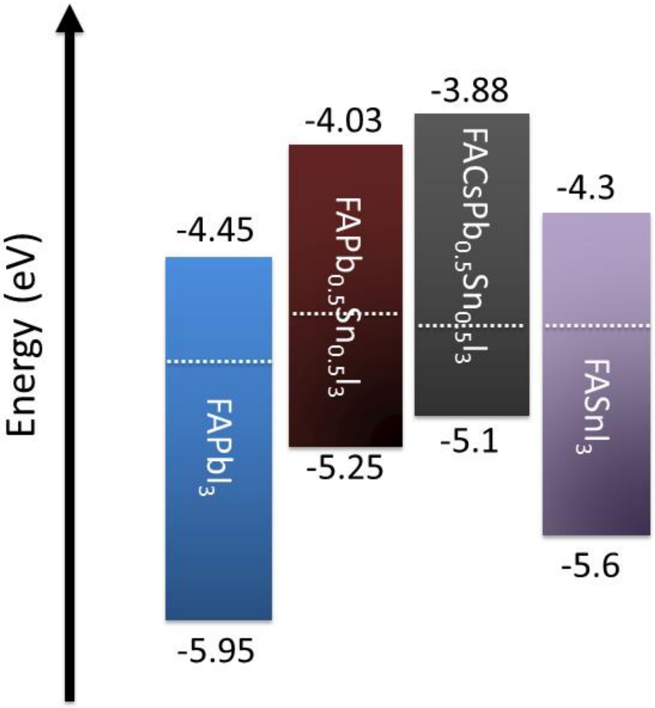

**Fig. S12: Energy level schematic for various compositions of $FASn_xPb_{1-x}I_3$ and $FA_{0.75}Cs_{0.25}Sn_{0.5}Pb_{0.5}I_3$ as determined by UPS and XPS.** Dotted white lines indicate the determined position of the fermi level.

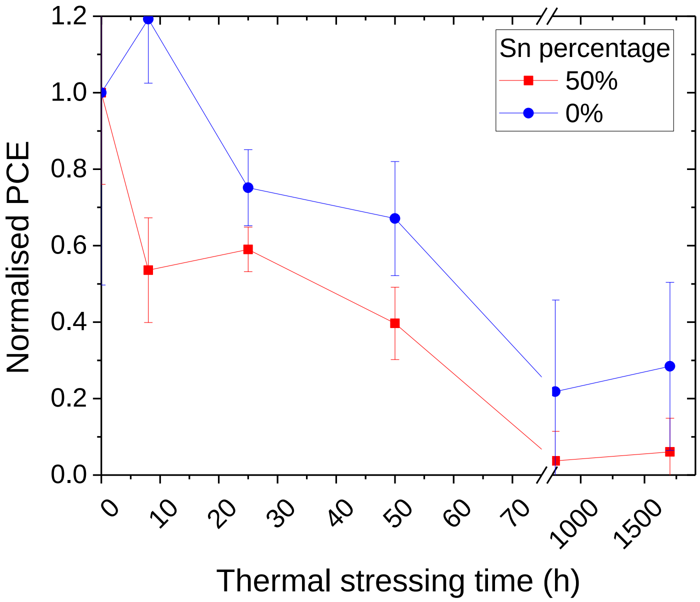

**Fig. S13. Device stability data measured over the course of many days at 85 °C in a $N_2$ glovebox.** Each point represents the average of 8 devices measured for the 0% material and 12 devices for the 50%. Error bars are determined from standard deviation. The pure Sn material tested degraded fully to 0% PCE before the first measurement at 8h. The 50% Sn:Pb material displays similar thermal stability performance to the pure Pb.

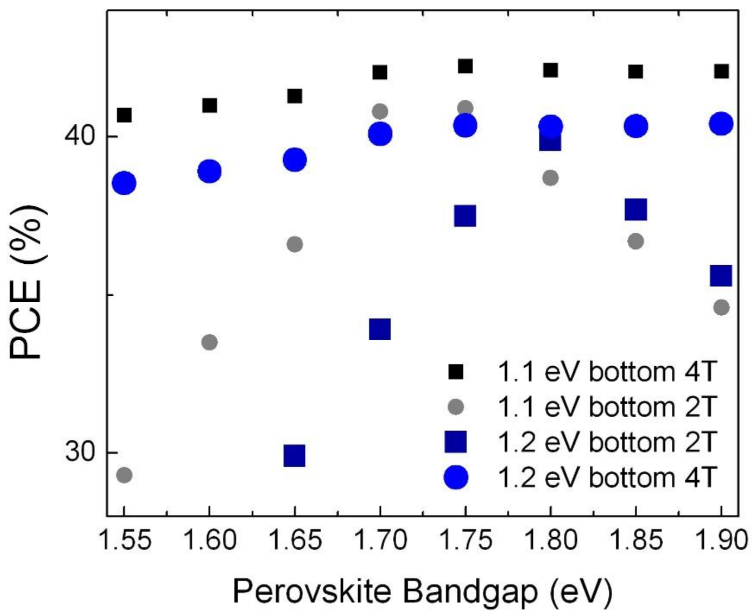

**Fig. S14: Calculated maximum efficiency for 2T and 4T configurations as a function of wide gap cell bandgap, for 1.1 (Si) and 1.2eV rear cells.** Absorption and reflection losses are ignored, we simply consider the two absorber layers and their maximum potential here.

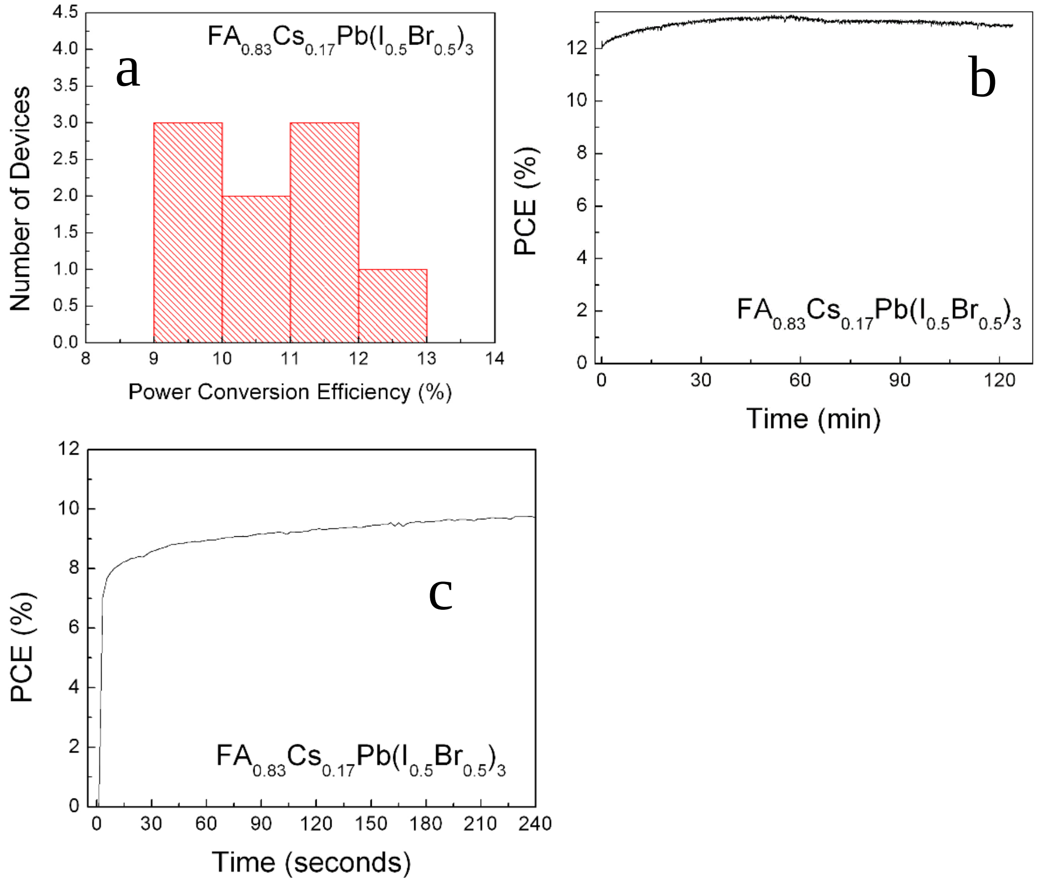

**Fig. S15. Wide gap single junctions.** a) Batch statistics of the 1.8eV $FA_{0.75}Cs_{0.25}Pb(I_{0.5}Br_{0.5})_3$, b) SPO of a 1.8eV solar cell with a solid Al electrode, and c) of the ITO contacted 1.8eV front cell presented in Figure 3.

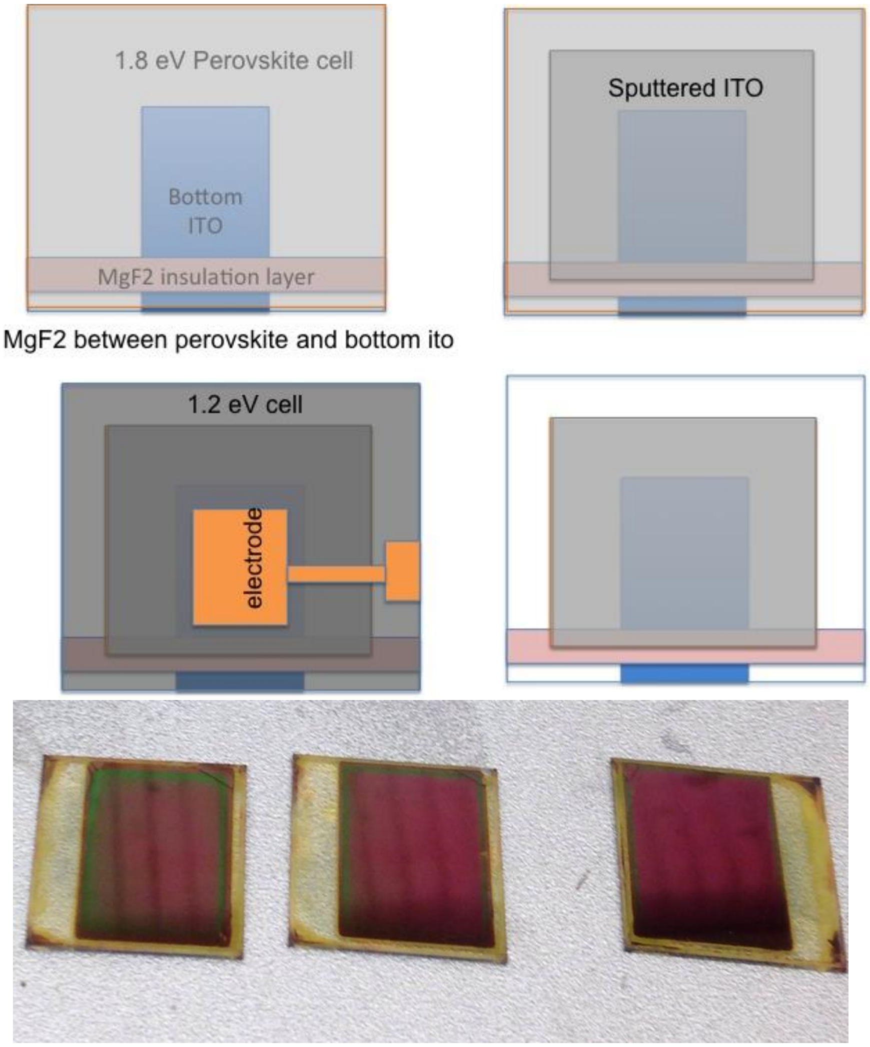

**Fig. S16. Schematic showing the fabrication of the 2T tandem.** A 1.8 eV cell is prepared on a patterned ITO substrate. A 100 nm $MgF_2$ strip is evaporated horizontally across the ITO, below the NiO and perovskite. ITO is sputtered on top of the 1.8eV cell. This protects the cell from damage when the PEDOT:PSS contact is deposited on top. The $MgF_2$ serves to insulate the sputtered ITO from the bottom ITO (on substrate) in case of any dissolution of the solar cell layers between. The 1.2 eV cell is then deposited on top of the PEDOT:PSS and finished with a gold or silver electrode. This design allows both cells to be contacted without any risk of shorting through either. The photo depicts several ITO covered 1.8eV devices on the hotplate after PEDOT:PSS deposition. The ITO layer clearly has protected the underlying perovskite while in areas where there is no ITO (around the rectangle) the perovskite has dissolved/degraded upon PEDOT:PSS deposition.

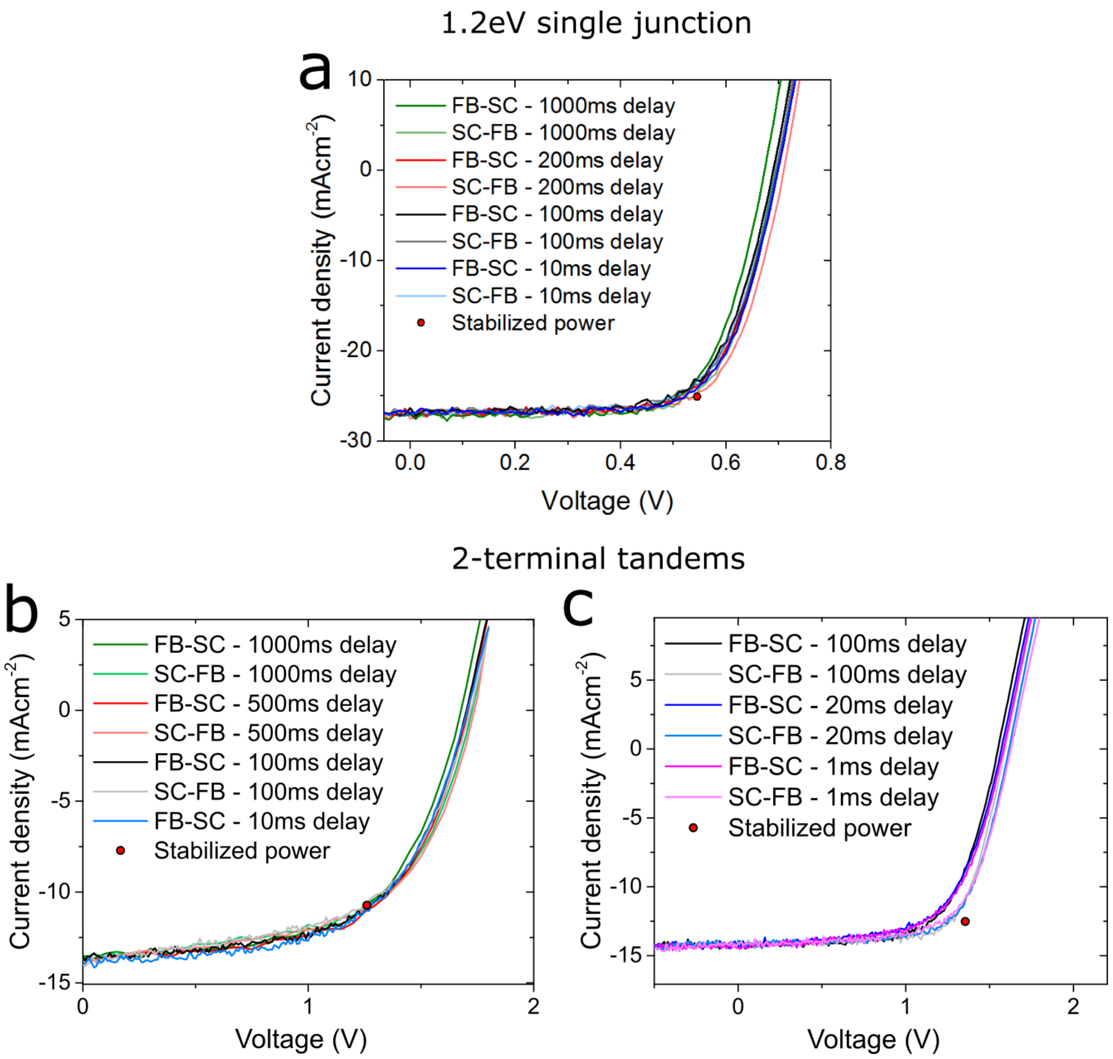

**Fig S17: Scan rate dependent hysteresis. a) in single junction $FA_{0.75}Cs_{0.25}Sn_{0.5}Pb_{0.5}I_3$ 1.2eV device, and b) and c) in 2T tandems.** The scan rate was varied by changing the hold (delay) time at each voltage, with steps of 0.005V; very little change in scans was seen at the different rates, and the forward and reverse scans are similar (FB-SC = forward bias to short circuit, and vice versa). The stabilized power output at the maximum power point is shown as a red circle in each plot. b) and c) show scan rate dependences for two different 2T tandems (with different efficiencies), to cover a wider range of delay times.

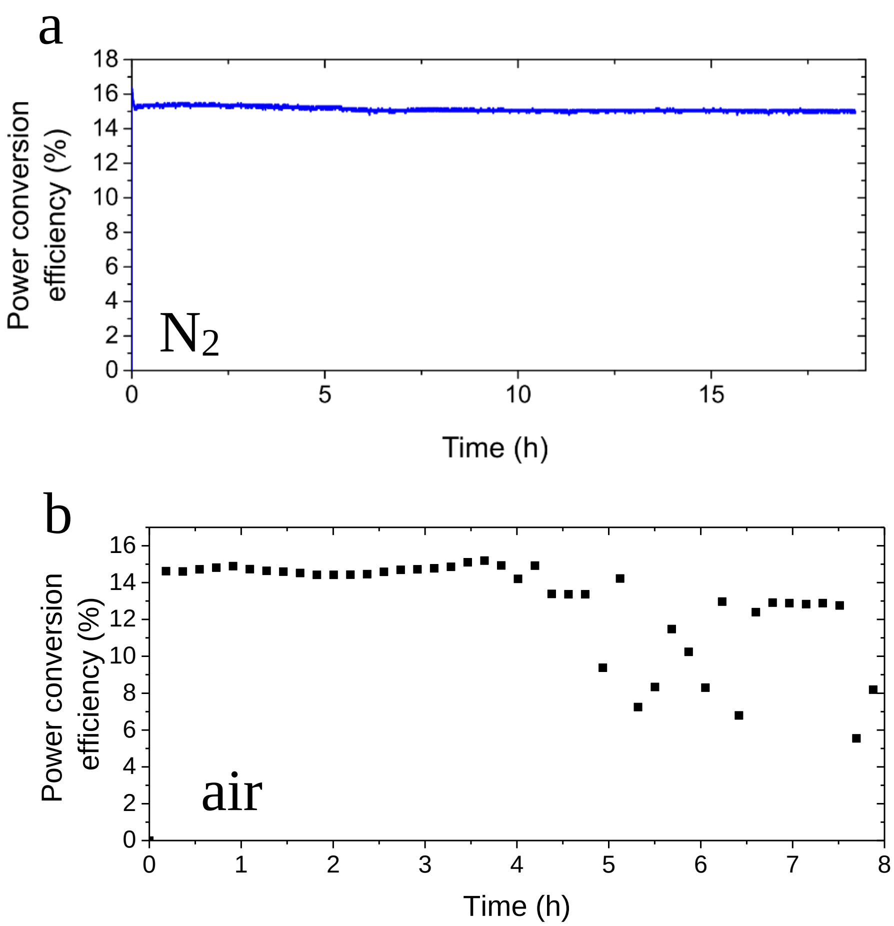

**Fig. S18: Long time maximum power point measurement for 2T tandem.** The device was measured under 100mWcm$^{-2}$ AM1.5G illumination in a) nitrogen and b) ambient air while tracking the MPP. The devices were not encapsulated.

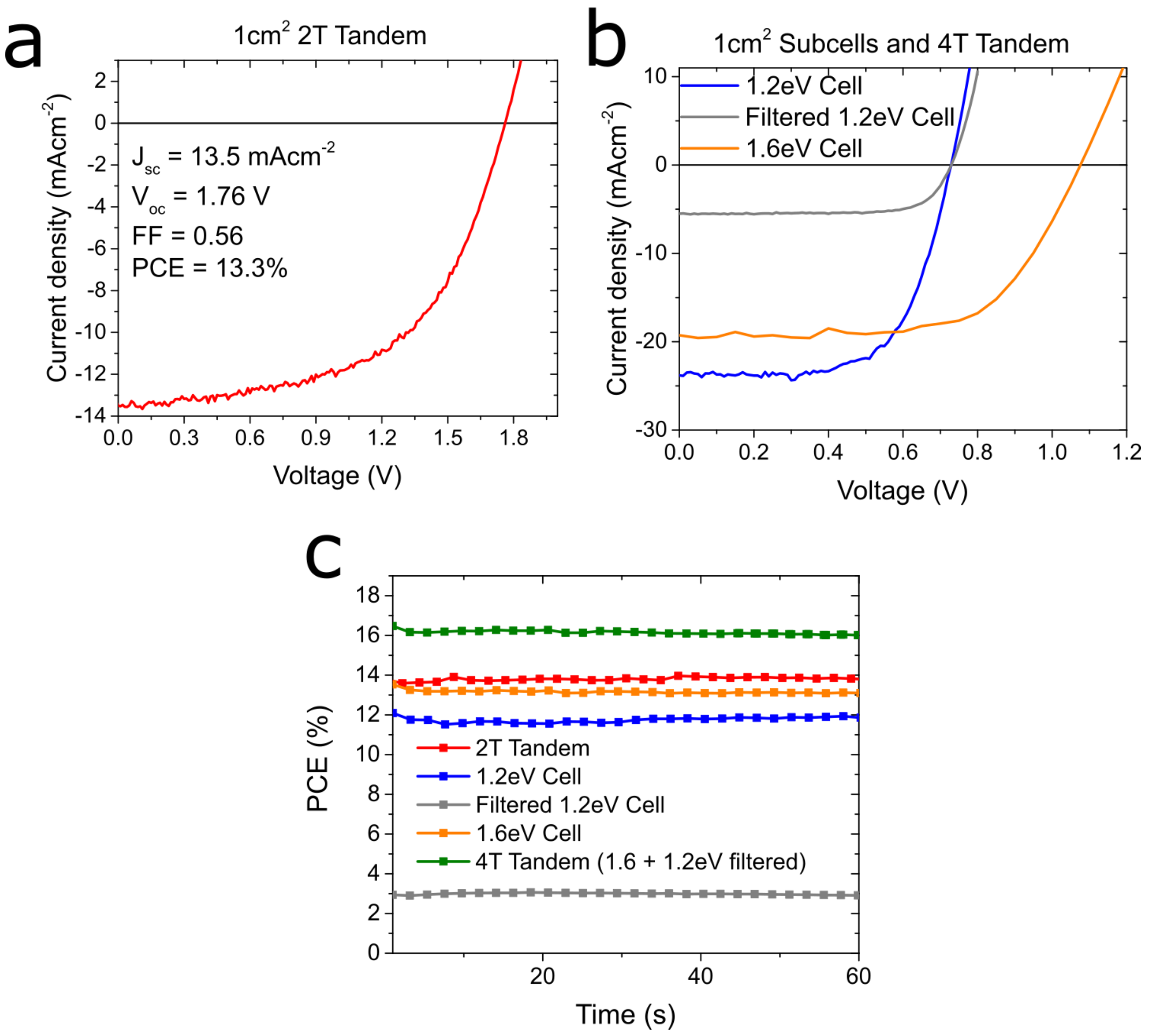

**Fig S19: Large area devices.** a) current-voltage characteristics for the 1cm$^2$ 2T tandem and b) the 1cm$^2$ 4T tandem and subcells described in the main text. c) Stabilized power output for the 1cm$^2$ devices. Values extracted from this data are given in the main text in Table 2.

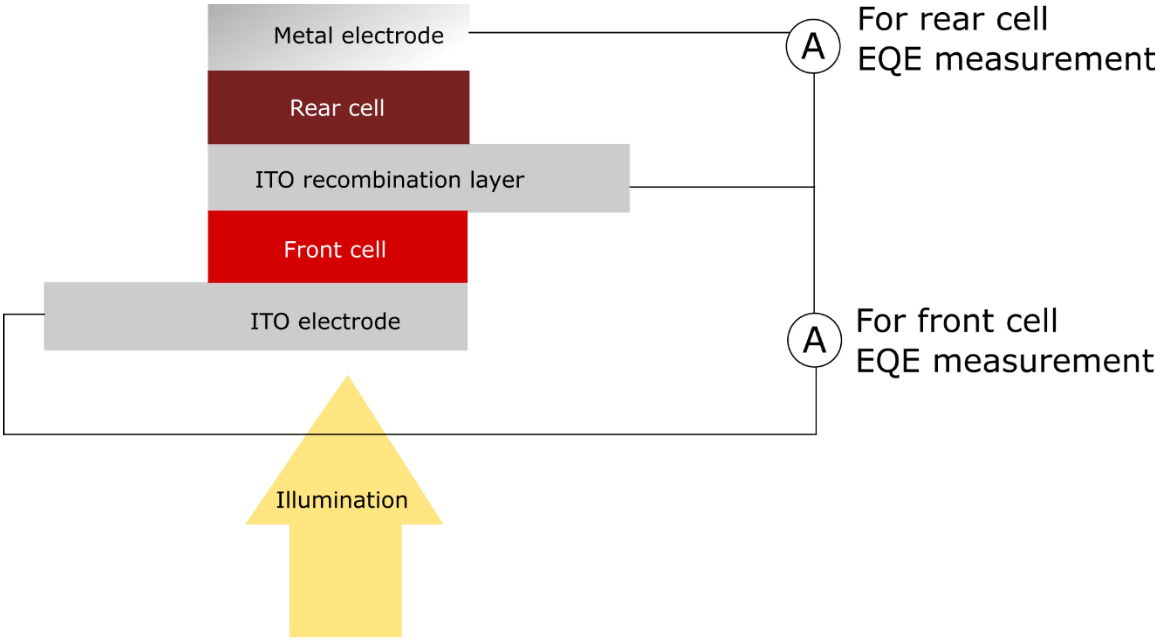

**Fig S20: EQE measurement.** Simple diagram showing the contacting setup used for measuring the EQE of each sub-cell. The ITO recombination layer allows facile contacting of each cell individually – the other cell is left uncontacted during measurement.

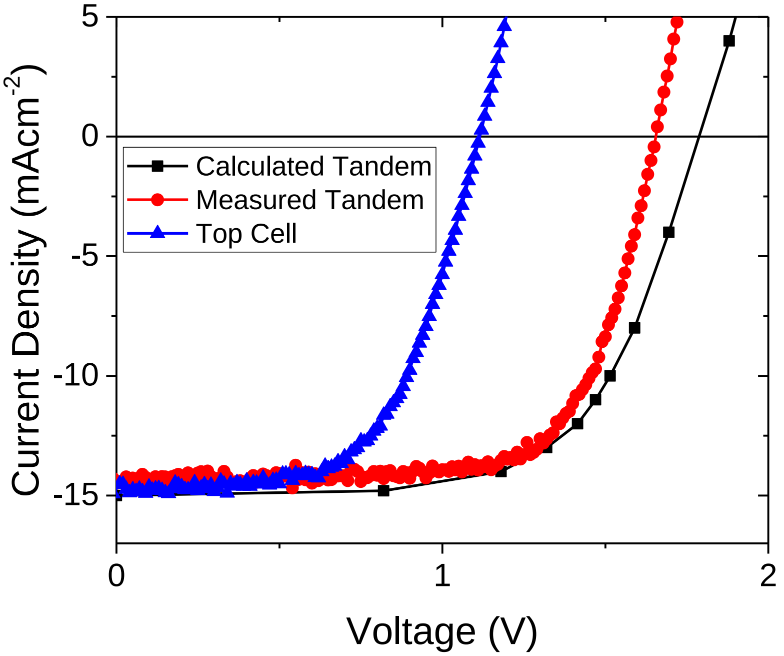

**Fig S21: Calculated tandem JV characteristics based on sub-cells.** By adding the voltages of the sub-cell data points when they generate the same current, we determine the expected 2T tandem JV curve (black). Here, the 1.2eV cell is assumed to follow ideal diode behavior so the photocurrent is simply adjusted to 15.8 mA cm$^{-2}$ since this will be the limiting current in the tandem. We see a good agreement between the expected and measured data, with a slightly lower voltage in the measured data. The measured JV curve for the 2T tandem generates 16.9% PCE and the calculated curve is in good agreement at 17.2%, demonstrating that our fabricated tandems are limited by the sub-cells not by monolithic processing concerns. The FF for the calculated curve is 0.64, greater than that of the top cell alone (0.58), as we discuss in the text.

## References and Notes

1. NREL, *Best Research-Cell Efficiencies*, http://www.nrel.gov/ncpv/images/efficiency_chart.jpg (2016).

2. D. P. McMeekin, G. Sadoughi, W. Rehman, G. E. Eperon, M. Saliba, M. T. Hörantner, A. Haghighirad, N. Sakai, L. Korte, B. Rech, M. B. Johnston, L. M. Herz, H. J. Snaith, A mixed-cation lead mixed-halide perovskite absorber for tandem solar cells. *Science* **351**, 151–155 (2016). doi:10.1126/science.aad5845 Medline

3. N. K. Noel, S. D. Stranks, A. Abate, C. Wehrenfennig, S. Guarnera, A.-A. Haghighirad, A. Sadhanala, G. E. Eperon, S. K. Pathak, M. B. Johnston, A. Petrozza, L. M. Herz, H. J. Snaith, Lead-free organic-inorganic tin halide perovskites for photovoltaic applications. *Energy Environ. Sci.* **7**, 3061–3068 (2014). doi:10.1039/C4EE01076K

4. F. Hao *et al*., Solvent-mediated crystallization of $CH_3NH_3SnI_3$ films for heterojunction depleted perovskite solar cells. *J. Am. Chem. Soc.* **137**, 11445–11452 (2015).

5. F. Hao, C. C. Stoumpos, R. P. H. Chang, M. G. Kanatzidis, Anomalous band gap behavior in mixed Sn and Pb perovskites enables broadening of absorption spectrum in solar cells. *J. Am. Chem. Soc.* **136**, 8094–8099 (2014). doi:10.1021/ja5033259 Medline

6. L. Zhu, B. Yuh, S. Schoen, X. Li, M. Aldighaithir, B. J. Richardson, A. Alamer, Q. Yu, Solvent-molecule-mediated manipulation of crystalline grains for efficient planar binary lead and tin triiodide perovskite solar cells. *Nanoscale* **8**, 7621–7630 (2016). doi:10.1039/C6NR00301J Medline

7. Z. Yang, A. Rajagopal, C. C. Chueh, S. B. Jo, B. Liu, T. Zhao, A. K. Jen, Stable low-bandgap Pb-Sn binary perovskites for tandem solar cells. *Adv. Mater.* (2016). doi:10.1002/adma.201602696 Medline

8. Y. Zhou, M. Yang, W. Wu, A. L. Vasiliev, K. Zhu, N. P. Padture, Room-temperature crystallization of hybrid-perovskite thin films via solvent-solvent extraction for high-performance solar cells. *J. Mater. Chem. A Mater. Energy Sustain.* **3**, 8178–8184 (2015). doi:10.1039/C5TA00477B

9. See supplementary materials on *Science* Online.

10. C. C. Stoumpos, C. D. Malliakas, M. G. Kanatzidis, Semiconducting tin and lead iodide perovskites with organic cations: Phase transitions, high mobilities, and near-infrared photoluminescent properties. *Inorg. Chem.* **52**, 9019–9038 (2013). doi:10.1021/ic401215x Medline

11. J. Im, C. C. Stoumpos, H. Jin, A. J. Freeman, M. G. Kanatzidis, Antagonism between spin-orbit coupling and steric effects causes anomalous band gap evolution in the perovskite photovoltaic materials $CH_3NH_3Sn_{1-x}Pb_xI_3$. *J. Phys. Chem. Lett.* **6**, 3503–3509 (2015). doi:10.1021/acs.jpclett.5b01738 Medline

12. L. M. Herz, Charge-carrier dynamics in organic-inorganic metal halide perovskites. *Annu. Rev. Phys. Chem.* **67**, 65–89 (2016). doi:10.1146/annurev-physchem-040215-112222

13. W. Rehman, R. L. Milot, G. E. Eperon, C. Wehrenfennig, J. L. Boland, H. J. Snaith, M. B. Johnston, L. M. Herz, Charge-carrier dynamics and mobilities in formamidinium lead

mixed-halide perovskites. *Adv. Mater.* **27**, 7938–7944 (2015). doi:10.1002/adma.201502969 Medline

14. E. S. Parrott, R. L. Milot, T. Stergiopoulos, H. J. Snaith, M. B. Johnston, L. M. Herz, Effect of structural phase transition on charge-carrier lifetimes and defects in $CH_3NH_3SnI_3$ perovskite. *J. Phys. Chem. Lett.* **7**, 1321–1326 (2016). doi:10.1021/acs.jpclett.6b00322 Medline
15. M. B. Johnston, L. M. Herz, Hybrid perovskites for photovoltaics: Charge-carrier recombination, diffusion, and radiative efficiencies. *Acc. Chem. Res.* **49**, 146–154 (2016). doi:10.1021/acs.accounts.5b00411 Medline
16. P. Docampo, J. M. Ball, M. Darwich, G. E. Eperon, H. J. Snaith, Efficient organometal trihalide perovskite planar-heterojunction solar cells on flexible polymer substrates. *Nat. Commun.* **4**, 2761 (2013). doi:10.1038/ncomms3761 Medline
17. Z. Li, M. Yang, J.-S. Park, S.-H. Wei, J. J. Berry, K. Zhu, Stabilizing perovskite structures by tuning tolerance factor: formation of formamidinium and cesium lead iodide solid-state alloys. *Chem. Mater.* **28**, 284–292 (2016). doi:10.1021/acs.chemmater.5b04107
18. J.-W. Lee, D.-H. Kim, H.-S. Kim, S.-W. Seo, S. M. Cho, N.-G. Park, Formamidinium and cesium hybridization for photo- and moisture-stable perovskite solar cell. *Adv. Energy Mater.* **5**, 1501310 (2015). doi:10.1002/aenm.201501310
19. C. Yi *et al*., Entropic stabilization of mixed A-cation ABX 3 metal halide perovskites for high performance perovskite solar cells. *Energy Environ. Sci.* **2**, 303 (2016).
20. T. K. Todorov, O. Gunawan, T. Gokmen, D. B. Mitzi, Solution-processed Cu $(In,Ga)(S,Se)_2$ absorber yielding a 15.2% efficient solar cell. *Prog. Photovolt. Res. Appl.* **21**, 82–87 (2013). doi:10.1002/pip.1253
21. P. Schulz, E. Edri, S. Kirmayer, G. Hodes, D. Cahen, A. Kahn, Interface energetics in organo-metal halide perovskite-based photovoltaic cells. *Energy Environ. Sci.* **7**, 1377 (2014). doi:10.1039/c4ee00168k
22. C. Wang, C. Wang, X. Liu, J. Kauppi, Y. Shao, Z. Xiao, C. Bi, J. Huang, Y. Gao, Electronic structure evolution of fullerene on $CH_3NH_3PbI_3$. *Appl. Phys. Lett.* **106**, 111603 (2015). doi:10.1063/1.4916079
23. H. J. Snaith, Estimating the maximum attainable efficiency in dye-sensitized solar cells. *Adv. Funct. Mater.* **20**, 13–19 (2010). doi:10.1002/adfm.200901476
24. M. A. Green, K. Emery, Y. Hishikawa, W. Warta, E. D. Dunlop, Solar cell efficiency tables (version 45). *Prog. Photovolt. Res. Appl.* **23**, 1–9 (2015). doi:10.1002/pip.2573
25. F. Hao, C. C. Stoumpos, D. H. Cao, R. P. H. Chang, M. G. Kanatzidis, Lead-free solid-state organic–inorganic halide perovskite solar cells. *Nat. Photonics* **8**, 489–494 (2014). doi:10.1038/nphoton.2014.82
26. T. Leijtens, G. E. Eperon, N. K. Noel, S. N. Habisreutinger, A. Petrozza, H. J. Snaith, Stability of metal halide perovskite solar cells. *Adv. Energy Mater.* **5**, 1500963 (2015). doi:10.1002/aenm.201500963

27. B. Conings, J. Drijkoningen, N. Gauquelin, A. Babayigit, J. D'Haen, L. D'Olieslaeger, A. Ethirajan, J. Verbeeck, J. Manca, E. Mosconi, F. D. Angelis, H.-G. Boyen, Intrinsic thermal instability of methylammonium lead trihalide perovskite. *Adv. Energy Mater.* **5**, 1500477 (2015). doi:10.1002/aenm.201500477

28. D. Bi, W. Tress, M. I. Dar, P. Gao, J. Luo, C. Renevier, K. Schenk, A. Abate, F. Giordano, J.-P. Correa Baena, J.-D. Decoppet, S. M. Zakeeruddin, M. K. Nazeeruddin, M. Grätzel, A. Hagfeldt, Efficient luminescent solar cells based on tailored mixed-cation perovskites. *Sci. Adv.* **2**, e1501170 (2016). doi:10.1126/sciadv.1501170 Medline

29. K. A. Bush, C. D. Bailie, Y. Chen, A. R. Bowring, W. Wang, W. Ma, T. Leijtens, F. Moghadam, M. D. McGehee, Thermal and environmental stability of semi-transparent perovskite solar cells for tandems enabled by a solution-processed nanoparticle buffer layer and sputtered ITO electrode. *Adv. Mater.* **28**, 3937–3943 (2016). doi:10.1002/adma.201505279 Medline

30. J. Werner, C.-H. Weng, A. Walter, L. Fesquet, J. P. Seif, S. De Wolf, B. Niesen, C. Ballif, Efficient monolithic perovskite/silicon tandem solar cell with cell area >1 $cm^2$. *J. Phys. Chem. Lett.* **7**, 161–166 (2016). doi:10.1021/acs.jpclett.5b02686 Medline

31. S. Albrecht, M. Saliba, J. P. Correa Baena, F. Lang, L. Kegelmann, M. Mews, L. Steier, A. Abate, J. Rappich, L. Korte, R. Schlatmann, M. K. Nazeeruddin, A. Hagfeldt, M. Grätzel, B. Rech, Monolithic perovskite/silicon-heterojunction tandem solar cells processed at low temperature. *Energy Environ. Sci.* **9**, 81–88 (2015). doi:10.1039/C5EE02965A

32. A. Hadipour, B. de Boer, J. Wildeman, F. B. Kooistra, J. C. Hummelen, M. G. R. Turbiez, M. M. Wienk, R. A. J. Janssen, P. W. M. Blom, Solution-processed organic tandem solar cells. *Adv. Funct. Mater.* **16**, 1897–1903 (2006). doi:10.1002/adfm.200600138

33. D. Sabba, H. K. Mulmudi, R. R. Prabhakar, T. Krishnamoorthy, T. Baikie, P. P. Boix, S. Mhaisalkar, N. Mathews, Impact of anionic $Br^-$ substitution on open circuit voltage in lead free perovskite ($CsSnI_{3-x}Br_x$) solar cells. *J. Phys. Chem. C* **119**, 1763–1767 (2015). doi:10.1021/jp5126624

34. T. M. Koh, T. Krishnamoorthy, N. Yantara, C. Shi, W. L. Leong, P. P. Boix, A. C. Grimsdale, S. G. Mhaisalkar, N. Mathews, Formamidinium tin-based perovskite with low $E_g$ for photovoltaic applications. *J. Mater. Chem. A Mater. Energy Sustain.* **3**, 14996–15000 (2015). doi:10.1039/C5TA00190K

35. P. Giannozzi, S. Baroni, N. Bonini, M. Calandra, R. Car, C. Cavazzoni, D. Ceresoli, G. L. Chiarotti, M. Cococcioni, I. Dabo, A. Dal Corso, S. de Gironcoli, S. Fabris, G. Fratesi, R. Gebauer, U. Gerstmann, C. Gougoussis, A. Kokalj, M. Lazzeri, L. Martin-Samos, N. Marzari, F. Mauri, R. Mazzarello, S. Paolini, A. Pasquarello, L. Paulatto, C. Sbraccia, S. Scandolo, G. Sclauzero, A. P. Seitsonen, A. Smogunov, P. Umari, R. M. Wentzcovitch, QUANTUM ESPRESSO: A modular and open-source software project for quantum simulations of materials. *J. Phys. Condens. Matter* **21**, 395502 (2009). doi:10.1088/0953-8984/21/39/395502 Medline

36. J. P. Perdew, K. Burke, M. Ernzerhof, Generalized gradient approximation made simple. *Phys. Rev. Lett.* **77**, 3865–3868 (1996). doi:10.1103/PhysRevLett.77.3865 Medline

37. N. Troullier, J. L. Martins, Efficient pseudopotentials for plane-wave calculations. *Phys. Rev. B Condens. Matter* **43**, 1993–2006 (1991). doi:10.1103/PhysRevB.43.1993 Medline

38. J. P. Perdew, M. Ernzerhof, K. Burke, Rationale for mixing exact exchange with density functional approximations. *J. Chem. Phys.* **105**, 9982 (1996). doi:10.1063/1.472933

39. H. J. Snaith, How should you measure your excitonic solar cells? *Energy Environ. Sci.* **5**, 6513 (2012). doi:10.1039/c2ee03429h

40. S. Sista, Z. Hong, M. H. Park, Z. Xu, Y. Yang, High-efficiency polymer tandem solar cells with three-terminal structure. *Adv. Mater.* **22**, E77–E80 (2010). doi:10.1002/adma.200901624 Medline

41. J. B. Patel, R. L. Milot, A. D. Wright, L. M. Herz, M. B. Johnston, Formation dynamics of $CH_3NH_3PbI_3$ perovskite following two-step layer deposition. *J. Phys. Chem. Lett.* **7**, 96–102 (2016). Medline

42. C. Wehrenfennig, G. E. Eperon, M. B. Johnston, H. J. Snaith, L. M. Herz, High charge carrier mobilities and lifetimes in organolead trihalide perovskites. *Adv. Mater.* **26**, 1584–1589 (2014). doi:10.1002/adma.201305172 Medline

43. M. R. Filip, G. E. Eperon, H. J. Snaith, F. Giustino, Steric engineering of metal-halide perovskites with tunable optical band gaps. *Nat. Commun.* **5**, 5757 (2014). doi:10.1038/ncomms6757 Medline